Volume morphology of printable solar cells

Volume morphology of printable solar cells

Printable polymer or hybrid solar cells (PSCs) have the potential to become one of the leading technologies of the 21st century in conversion of sunlight to electrical energy. Because of their ease of processing from solution fast and low cost mass production of devices is possible in a roll-to-roll printing fashion. The performance of such printed devices, in turn, is determined to a large extent by the three-dimensional organization of the photoactive layer, i.e. layer where light is absorbed and converted into free electrical charges, and its contacts with the charge collecting electrodes. In this review I briefly introduce our current understanding of morphology-performance relationships in PSCs with specific focus on electron tomography as analytical tool providing volume information with nanometer resolution.

Joachim Loos
School of Physics and Astronomy, University of Glasgow, Glasgow G12 8QQ, Scotland, United Kingdom, and Department of Chemical Engineering and Chemistry, Eindhoven University of Technology, P.O. Box 513, NL-5600 MB Eindhoven, The Netherlands, and Dutch Polymer Institute, P.O. Box 902, NL-5600 AX Eindhoven, The Netherlands
E-mail: joachim.loos@glasgow.ac.uk

Beside conventional silicon-based solar cells and promising technology developments of e.g. dye sensitized and CdTe based solar cells[1], in recent years, an alternative type of solar cells has been intensively studied, viz. thin film devices printable from purely organic or hybrid solutions/dispersions using semi-conducting polymers like poly phenylene-vinylene, polythiopene, or polyfluorene, for light absorption and charge transport[2-4]. Such printable solar cells (PSCs) have a distinct advantage over inorganic counterparts, viz. their fast and low-cost manufacturing process: they can be fabricated by processing polymers, eventually together with other organic and/or inorganic materials, in solution/dispersion and depositing them by printing or coating in a roll-to-roll fashion like newspapers. Thanks to the speed and ease of this manufacturing process, the energy payback time of PSCs may, according to some estimates, be limited to months to about a year only[5,6]. Additional advantages include lightweight and flexibility of organic materials, enabling fast and easy applications on e.g. curved surfaces and thus freedom of design.

Most research on PSCs relates to increasing efficiency in converting light to electricity, and as current record an efficiency of 8.1% has recently been certified for a lab-scale device[7]. Although substantial

ISSN:1369 7021 © Elsevier Ltd 2010

lower than commercial amorphous silicon solar cells, the much lower cost (and energy) of production would more than offset the difference in efficiency for most applications.

PSCs are still in the research and development phase; however, first commercial products recently were introduced to the market[8]. To bring them closer to the stage of practical efficient devices, several issues should still be addressed, including further improvements of their efficiency and lifetime.

How does a PSC work?

In a typical printable solar cell (Fig. 1), light absorption in the photoactive layer creates strongly bound excitons (coulombic bound electron-hole pairs), which can dissociate into free charges only at electron donor/acceptor interfaces by rapid electron transfer from the donor to the acceptor material[9,10]. The morphological challenge is to generate in the photoactive layer a maximized interface between donor and acceptor materials within its whole volume for maximum exciton dissociation, and to ensure the creation of continuous, preferably short, pathways of both donor and acceptor materials for charge transport to the respective electrodes; such morphology is a so-called bulk heterojunction[11,12]. As a consequence, the performance of PSCs depends critically on the nanoscale organization of the photoactive layer and its interfaces with the charge collecting electrodes. Beside the right choice of the donor/acceptor combination, features that influence morphology formation in the photoactive layer are the solvent used (solubility, boiling temperature, etc.)[13-15], solvent additives[16], compound ratio[17,18], and annealing after film forming[19-23], to name but a few.

To understand critical parameters determining morphology formation and to link the thus formed morphology of the photoactive layer with the performance of bulk-heterojunction solar cells, it is essential to have information in terms of volume organization of the photoactive layer and its interfaces with the electrodes. The thin-film nature of the photoactive layers with typical thicknesses of about 100-200 nm and the request for local morphology information make high-resolution microscopy techniques essential tools for morphology characterization. In this context, transmission electron microscopy (TEM) is one of the most powerful techniques. Using conventional TEM imaging of structures and their surfaces/interfaces with lateral resolution down to sub-nanometer scale, and the simultaneous analysis of the internal organization of these structures by means of electron diffraction and dark field imaging are well-established techniques in materials science. However, conventional TEM provides mainly morphological information on the lateral organization of the thin-film specimens under investigation by acquisition of two-dimensional (2D) projections through the whole volume of the photoactive layer.

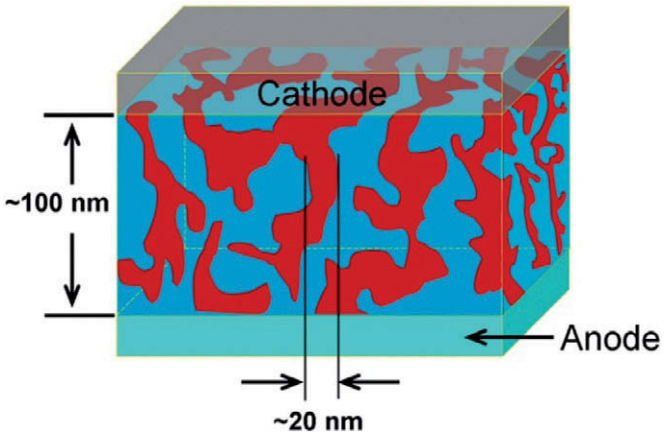

Fig. 1 Schematic 3D representation of a bulk heterojunction (electron donor and acceptor constituents in different colors) with top and bottom electrodes (Reprinted with permission from[4]. © (2007) American Chemical Society).

Electron tomography

The technique that supplies the required volume information with nanometer resolution is electron tomography (ET)[24-29]. Tomography, in its old Greek meaning, refers to a technique to reconstruct a section of an object, which is an inner section as opposed to surfaces. Since then tomography has become associated with mapping of inner sections across an object and therefore refers to a three-dimensional reconstruction method. Nowadays, tomography essentially means to reconstruct the three-dimensional structure of objects from a series of two-dimensional projections[30].

The best known example of a tomography technique is the X-ray CAT (computer-aided tomography or computed axial tomography) scanner you can find nowadays in any hospital as ubiquitous tool for diagnostic medicine[31]. Computer tomography allows the complete 3D internal structure of an object to be reconstructed from a set of 2D projections taken at different angular settings, without imposing any a priori assumptions or requirements regarding the symmetry of the object[25].

ET is based on the same principle: a series of 2D projections is taken by TEM at different angles by tilting the specimen with respect to the electron beam (Fig. 2). The tilt series thus obtained containing normally more than 100 images of the same specimen spot is then carefully aligned and used to reconstruct a 3D image of the specimen with nanometer resolution by back projection algorithms[32-34]. The outcome of electron tomography can be used voxel by voxel (a contraction of "volume pixel") to study in detail the specimen's volume morphological organization.

Two examples on PSC volume analysis by ET

After this brief introduction to PSC and ET, I like to present exemplary recent morphology studies we have performed with the help of ET on two bulk heterojunction systems: poly(3-hexylthiophene) (P3HT) as a donor and the fullerene derivative (6,6)-phenyl C_{61} butyric acid methyl ester (PCBM) as acceptor as currently one of the most successful

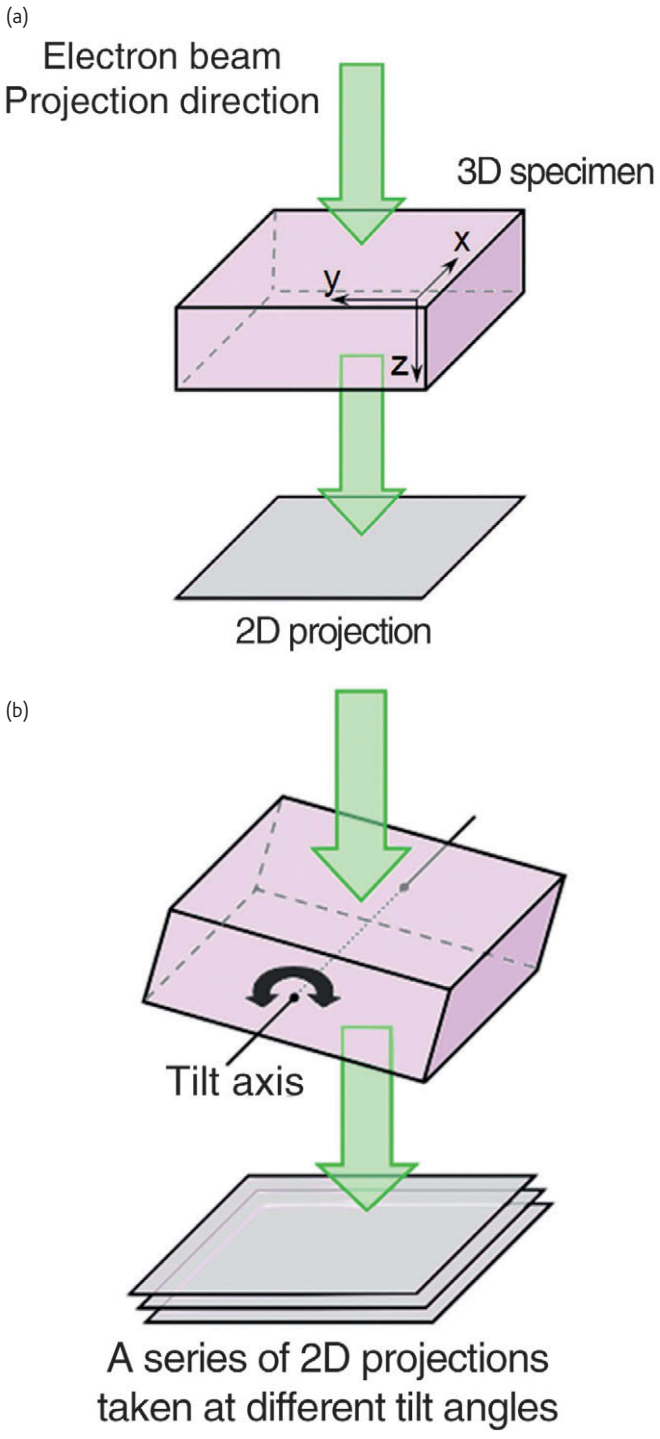

Fig. 2 Principles of a) conventional TEM imaging and b) electron tomography. A TEM image is basically a 2D projection taken of a 3D specimen under investigation: it gives no clear information on the morphological organization in z-direction and may be difficult to interpret in case of complex structures. In electron tomography, a series of such 2D projections is taken at different tilting angles by tilting the specimen along the tilt axis inside the TEM column, usually in the range of at least ±70°. The tilt series is later used to reconstruct the 3D image of the specimen (Reprinted with permission from[29]. © (2010) Wiley-VCH).

electron donor/acceptor combinations in terms of efficiency and long term stability, and the hybrid system P3HT as electron donor and ZnO as acceptor, on which we have performed in depth quantification of the nanoscale volume organization and related it to the performance of corresponding devices.

The current standard system for PSC: P3HT/PCBM

The high efficiency of devices based on a P3HT/PCBM bulk heterojunction photoactive layer can be related to the intrinsic properties of the two components. Regioregular P3HT can self-assemble into fibrillar structures with about 20 nm width and micrometer length and high crystalline order [35]. Because of close π-π stacking efficient interchain transport of charge carriers is achieved and the hole mobility in P3HT is high (up to ~1×10^{-4} cm^2 V^{-1} s^{-1})[36]. Moreover, in thin films interchain interactions of the P3HT nanofibers cause a red shift of the optical absorption, which provides an improved overlap with the solar emission. The second component, PCBM, is a C_{60} fullerene derivative with an electron mobility of ~1×10^{-3} cm^2 V^{-1} s^{-1}[36,37]. Compared to C_{60}, the solubility of PCBM in organic solvents is greatly improved, which allows the utilization of film deposition techniques requiring high-concentrated solution. Also PCBM can crystallize and control of nucleation and growth kinetics allows the adjustment of the crystal size and overall morphology. However, continuous crystallization may result in single crystals with micrometer sizes[38].

Results of the volume reconstruction applied to as spin-coated and annealed P3HT/PCBM photoactive layers are shown as snapshots in Figs. 3a-c. The volume data demonstrate evidently the presence of 3D nanoscale networks of both the P3HT nanofibers and PCBM. In the volume data clear indication for inclination of the crystalline P3HT nanofibers is seen so that genuine 3D rather than 2D networks are created. This guarantees excellent hole charge transport from any place within the photoactive layer to the hole collecting electrode (Fig. 3d).

By going slice by slice through the reconstructed volume of P3HT/PCBM films annealed for 20 min at 130 °C, the amount of crystalline P3HT nanofibers can be quantified in relation to the actual z-position within the photoactive layer. We have quantified such P3HT concentration gradients with respect to the thickness of the photoactive layer. As evident from Fig. 4, there is enrichment of crystalline P3HT nanofibers in the lower part of the layer close to the hole collecting electrode and, correspondingly, enrichment of PCBM close to the top (electron collecting) electrode for film thicknesses of 50 and 100 nm: a situation that is beneficial for collection of free charges. However, we found for thicker photoactive layers a homogeneous concentration distribution of P3HT and PCBM throughout the entire layer thickness. The same trend is observed in case of P3HT/PCBM layers obtained by solvent assisted annealing for 3 h[39].

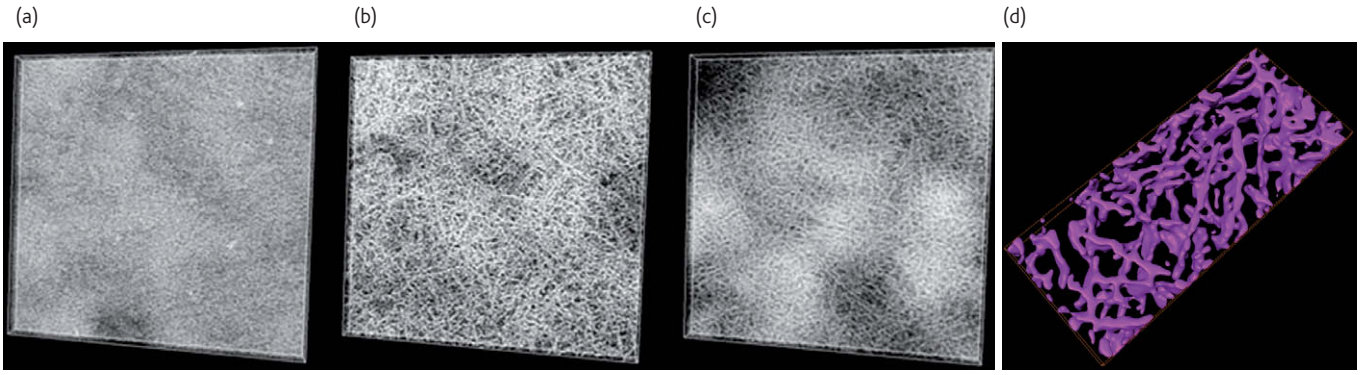

Fig. 3 Results of TEM tomography, a)-c) Snapshots of a reconstructed 3D volume of P3HT/PCBM photoactive layers: a) as spin-coated, b) thermally annealed and c) solvent assisted annealed for 3 h; The volume dimensions are about 1700 nm × 1700 nm × 100 nm; d) representation of the three-dimensional network of P3HT nanofibers formed in a thermally annealed P3HT/PCBM layer.

Further, it should be noted that only crystalline P3HT nanofibers are accounted for in this 3D morphology analysis since they have the required contrast with PCBM and get readily visualized in TEM imaging. Based on density values of P3HT and PCBM and a 1/1 weight ratio of these components in the photoactive layer in our experiments, P3HT should occupy *ca.* 58% of the total volume of the layer. From the plot presented in Fig. 4, we can estimate for the 100 nm thin film that approximately 35% of the layer volume is actually made up of crystalline P3HT nanofibers, which indicates a high crystallinity of about 60% for the P3HT.

In summary, the annealing treatment induces the formation of nanoscale interpenetrating networks of P3HT nanofibers and PCBM nanocrystals with favorable gradients within the thickness of the layer for the thinner specimens. These changes in the 3D volume organization of the P3HT/PCBM photoactive layer are paramount for obtaining high efficiency PSCs. Indeed, characterization of corresponding PSCs shows that values of the short-circuit current density (J_{sc}), the open circuit voltage (V_{oc}) and fill factor all increase substantially after thermal or solvent assisted annealing but stay unchanged at low level for the 200 nm sample. The overall efficiencies (not corrected for spectral mismatch and without performing device optimization) of devices with 100 nm thin photoactive layer almost doubled from 2.0% for as spin-coated P3HT/PCBM devices up to 3.8% for annealed devices[39,40].

Potential reasons for the vertical segregation of P3HT are currently still under debate[41]. Other studies based on modeling of data obtained by variable-angle spectroscopic ellipsometry (VASE)[42] and on X-ray Photoelectron Spectroscopy (XPS)[43] suggested that PCBM is preferentially concentrated on the bottom of the P3HT/PCBM films and that the potential reason for this is the high surface energy of the PEDOT:PSS layer.

However, because our ET data clearly demonstrate different sorts of vertical gradients in P3HT/PCBM films of varying thickness deposited on the same PEDOT:PSS substrate dismiss the key role of

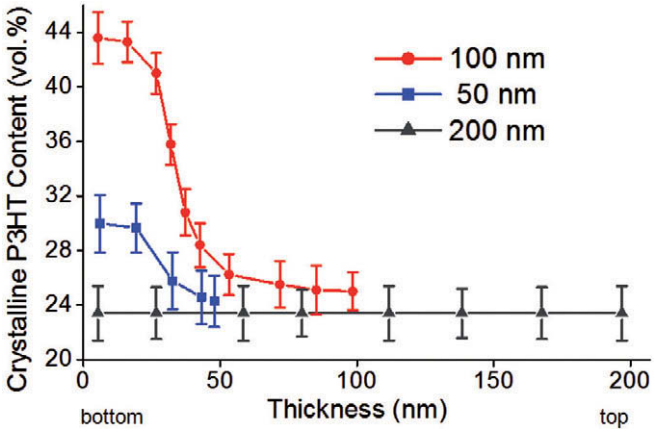

Fig. 4 Quantification of the crystalline P3HT nanofibers distribution through the thickness of the thermally annealed (TA) P3HT/PCBM photoactive layers: 50 nm, 100 nm and 200 nm thick. The thickness of 0 nm corresponds to the bottom side of the layer, i.e. the one next to the hole collecting PEDOT:PSS / ITO electrode. (Reprinted with permission from[40]. © (2009) American Chemical Society).

the underlying substrate's surface energy for formation of vertical gradients. Based on our results we believe that existence and type of compositional gradient strongly is determined by thermodynamic aspects of the interacting components, and more particular by the kinetic aspects involved during film and morphology formation. Main parameters influencing the organization of the film are different solution viscosity, different time it takes for the solvent to evaporate and eventual differences in local solvent concentration. These aspects have a direct impact on how long the macromolecules are mobile in the given solution/dispersion, on eventual precipitation of components depending on local variations in solvent concentration, and thus on formation of nuclei and subsequent growth and distribution of (nano)crystals throughout the photoactive layer during film formation. Therefore, molecular characteristics of the components such as molecular weight and regioregularity, and the chosen processing route strongly determine the nanoscale organization within

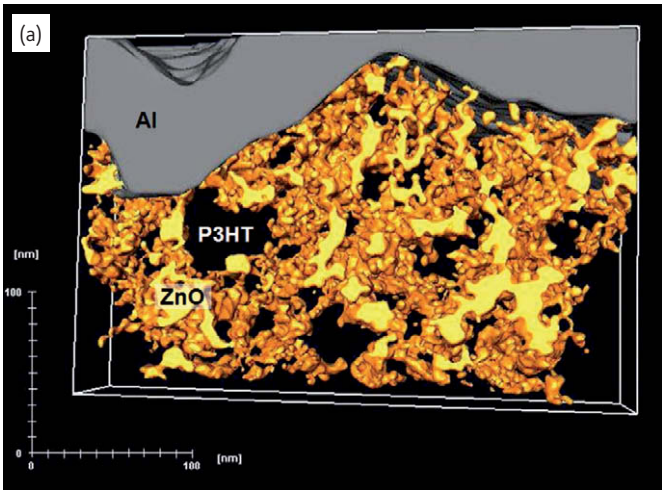

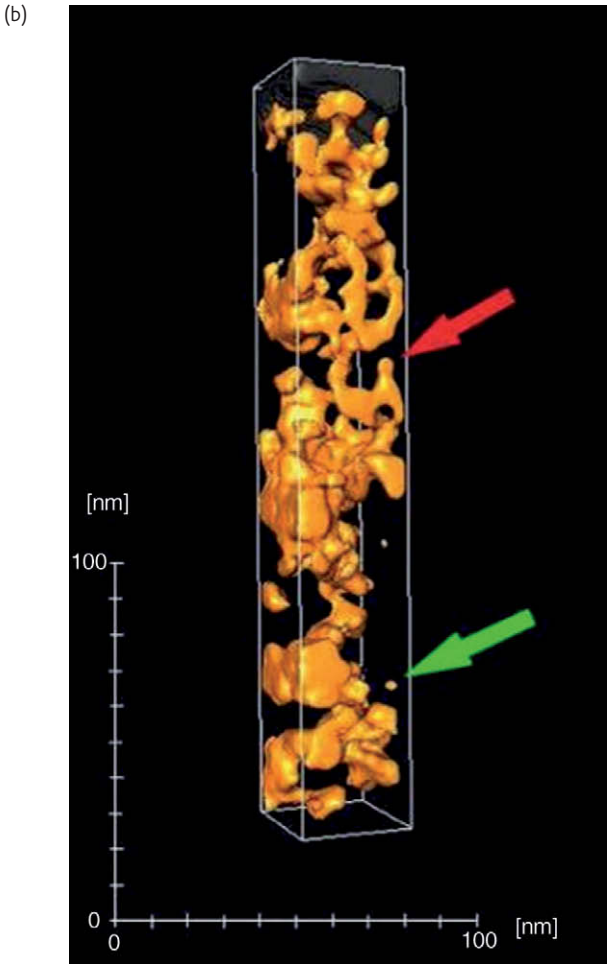

Fig. 5 a) Reconstructed volume of a cross-section of the P3HT/ZnO device with yellow ZnO domains in transparent P3HT matrix. The cross-section was obtained by using a focused ion beam (FIB) and is ca. 80 nm thick; b) the part of this volume with the green arrow indicating an isolated ZnO domain and the red arrow indicating a ZnO domain connected to the top, but not through a strictly rising path (Reprinted with permission from[51]. © (2009) Nature Publishing Group).

the photoactive layer and are responsible for the presence or absence of composition gradients.

Hybrid P3HT/ZnO PSCs

Beside purely organic bulk heterojunctions, PSCs can be processed also from mixtures of organic and inorganic materials. The concept of hybrid solar cells successfully has been demonstrated for systems based on semiconducting polymers as donor mixed with different inorganic materials such as CdSe[44,45], TiO_2[46,47] and ZnO[48-50], as acceptor. Potential advantages of the inorganic semiconductors are their high dielectric constant which facilitates carrier generation processes at the donor/acceptor interface, high carrier mobility, and their morphological stability within the photoactive layer upon thermal treatments.

The reasons for the lower efficiency of hybrid solar cells so far achieved as compared to the more efficient polymer/fullerene cells are only partly understood and need to be investigated to further increase their performance. Here we describe and analyze P3HT/ZnO solar cells that reach power conversion efficiencies of 2%[51]. In these solar cells the ZnO nanoparticles are prepared *in-situ* during the spin coating process from molecular precursors (diethylzinc). Electron tomography was applied to characterize the three-dimensional morphology of the P3HT/ZnO photoactive layers and their interfaces with the electrodes (Fig. 5), and thanks to the high contrast between the polymer and ZnO, the resulting 3D datasets could be easily analyzed in great detail. In the present case the elaborate 3D morphology quantification combined with photophysical characterization and device performance data provide clear insight into the role of the nanoscale 3D morphology in creating and transporting charges in the bulk-heterojunction photoactive layers[51].

In our study, from the accurate volume data obtained by ET we were able to determine the volume fraction of ZnO for photoactive layers with different thicknesses. In the two thickest layers, the experimental attained ZnO volume fraction (ca. 21 vol.-%) is close to the expected value of 19 vol.-%, based on the ratio of diethylzinc and P3HT in the initial spin-coating solution. However, the ZnO content in the thinnest layer is significantly lower at 13 vol.-%, which might be explained by the comparatively large fraction of the diethylzinc evaporating during spin-coating with the higher spin speed applied for this thin layer. The low ZnO content of this thinnest film accounts for the relatively large P3HT domains we have observed in our reconstructed volume data.

Further, we were able to calculate the spherical contact distances, which is defined as the distance from a certain voxel of one material to the nearest voxel of the other material. Because incident light is mainly absorbed by the polymer, excitons are mostly generated inside P3HT so that we focused on the distance distribution from P3HT to ZnO. Fig. 6 shows the probability to find P3HT at a certain shortest distance to a ZnO domain. For the thicker films, for most P3HT locations the distance to the interface with ZnO lies well within a shortest distance of 10 nm, which is about the exciton diffusion length and thus

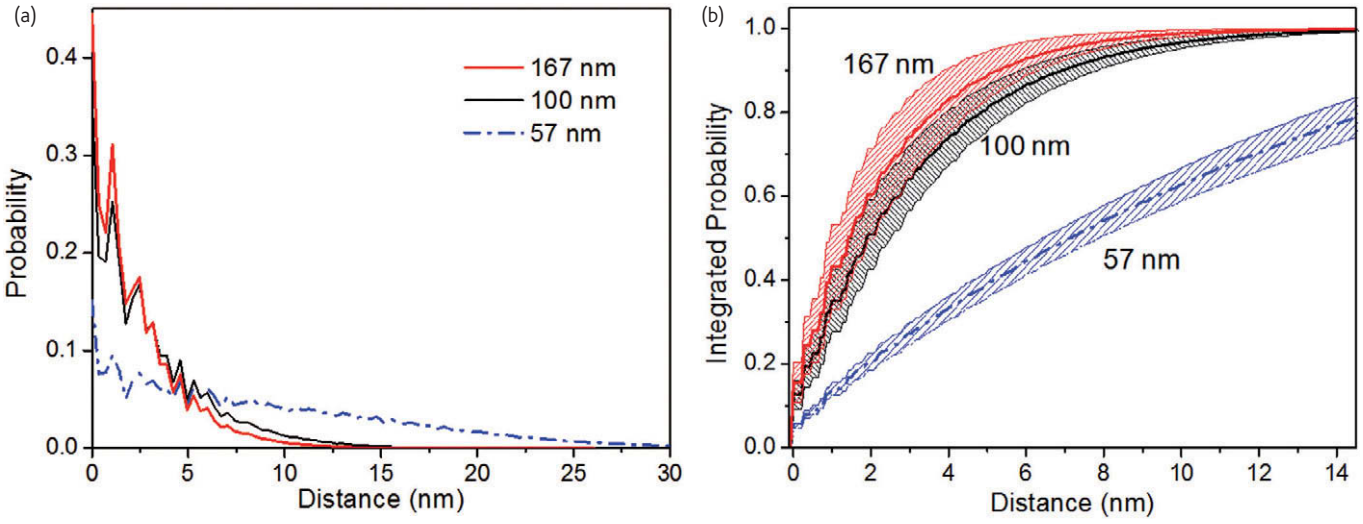

Fig. 6 Statistical analysis of the 3D morphology: a) Distribution of the probability to find a P3HT voxel at a certain distance from a ZnO domain for mixed P3HT/ZnO films of different thickness, calculated from 3D-datasets similar to the one displayed in Fig. 5; b) cumulative probability to have P3HT within a shortest distance to ZnO. The error margins indicated are obtained from the two most extreme thresholds possible for the binarization of the 3D data (Reprinted with permission from[51]. © (2009) Nature Publishing Group).

guarantees efficient free charge generation. On the other hand, the sample with the thinnest photoactive layer displays a large amount of polymer at shortest distances as high as 25 nm from an interface with ZnO. This analysis substantiates and quantifies that coarser phase separation is present in the thinnest layers.

Up to now, the presented data quantify the different degree of phase separation for the photoactive layers with different thickness, which directly reflect the efficiency of free charge generation. However, charges needs to be transported to the respective electrodes, too. Within a continuous phase, pathways may exist that do not continue into the direction toward the collecting electrode. Due to the macroscopic electric field over the photoactive layer in devices created by the difference of the work function of the electrodes, charges may be trapped inside so-called cul-de-sacs as shown in Fig. 5b, and are lost for collection. Therefore, we also determined the fraction of ZnO connected to the top through a strictly rising path. The calculated unidirectionally connected fraction of ZnO towards electron collecting Al electrode is still very high (93%) for the thinnest layer but reduces for thicker layers. The volume fraction of ZnO (with respect to the total volume of the photoactive layer) monotonously connected to the top electrode is, however, still higher in the thicker layers than in the thinnest one because of its significantly lower ZnO content. This implies that electron transport through thin P3HT/ZnO layers may be less efficient. However, as described above, there are also fewer charges to be transported in thin layers due to unfavorably large phase separation. Since the values of fill factor (that reflects the balanced transport of free charges) are comparable in all films, charge transport on the whole is unlikely to be less efficient in thin films.

To summarize, the hybrid system P3HT/ZnO presents a major advantage to study the relationship between 3D morphology and corresponding solar cell performance because 3D datasets provided by electron tomography can be straightforwardly analyzed in great detail, unattainable at the moment for polymer/fullerene blends. In our study, a quantitative analysis of the phase separation and percolation pathways was performed and used to explain the performance of P3HT/ZnO devices of different thickness. Looking at the combined effects of charge carrier generation and collection, we can conclude that the relative poor performance of thin P3HT/ZnO solar cells is related to inefficient charge generation as a result of the low ZnO content, to the coarse phase separation, and to the exciton losses impaired by the electrodes. For thicker photoactive layers charge generation is much more efficient, owing to a much more favourable phase separation. More information related to this study such as representative I(V)-curves and measurement conditions can be found in[51].

Concluding remarks and outlook

In a number of studies others and we have demonstrated that the performance of PSCs depends critically on the nanoscale organization and functionality of the photoactive layer, the interfaces with and type of the charge collecting electrodes, and the overall device architecture. For the latter, device performance can be improved e.g. by applying hole blocking layers[52], optical spacers to enhance light absorption in the layer of the same thickness[53,54] and by using the tandem cell architecture[55-57], where two printable photovoltaic cells are added in series. In a tandem cell, it is possible to combine two, or more, thinner (more efficient) active layers and to use semiconductors with different bandgaps for more efficient light harvesting. Besides, since individual cells are added in series, the open circuit voltage of a tandem cell is directly increased to the sum of the values of the corresponding individual cells.

Instrument Citation

TEM work was performed with Titan and Tecnai electron microscopes and the cross-sections shown in Fig. 5 were prepared with a Quanta 3D FEG, all instruments from FEI Co. (http://www.fei.com).

In general, morphology investigation of whole devices becomes more and more important because only by this way we can achieve realistic information on the entire system, the device; in particular this is of importance for aging or lifetime studies. Such studies mainly assess the long term performance of devices at elevated temperature but otherwise under inert conditions[58-60]. Commonly, during the ageing process, all of the parameters that can be extracted from an I(V) curve are recorded so that loss of performance can be identified. A similar approach is also applied for chemical degradation by exposing devices to oxygen, UV irradiation etc.[61]. Such studies document the changes in the device performance, but give little insight into the microscopic mechanism or the chemical and physical processes involved. In particular, changes in the interaction of the photoactive layer with the electrode material and local organization at the interfaces (e.g. delamination) have barely been considered.

In recent years we have demonstrated that Focused Ion Beam (FIB) is the tool of choice to prepare cross-sectional specimens out of full devices[51,62,63]. Such specimens are suitable for further analysis of e.g. interface roughness, presence of local phase separation, compositional gradients, chemical architecture of the interface and adhesion between the layers, to name but a few, after controlled aging experiments to identify critical parameters determining the lifetime of PSCs. Therefore, future volume organization studies certainly will focus on analysis of whole devices including the electrodes. mt

Acknowledgement

The author would like to use this opportunity to thank René Janssen, Martijn Wienk, Jan Kroon, Sjoerd Veenstra, Volker Schmidt and Xiaoniu Yang for fruitful discussions and fantastic cooperation, and the Dutch Polymer Institute (DPI) for superb support. In particular I like to thank Svetlana van Bavel for her excellent work which is the fundament of this article.

REFERENCES

1. www.gtmresearch.com/report/2009-cell-and-module-production-analysis.
2. Gunes, S., *et al., Chem Rev* (2007) **107**, 1324.
3. Hoppe, H., and Sariciftci, N. S., *Adv Polym Sci* (2008) **214**, 1.
4. Yang, X., and Loos, J., *Macromolecules* (2007) **40**, 1353.
5. Dennler, G., and Brabec, C. J., Socio-Economic Impact of Low-Cost PV Technologies. In *Organic Photovoltaics*, Brabec, C. J., *et al.,* (eds) Wiley-VCH, Weinheim, (2008) 531.
6. Roes, A. L., *et al., Prog Photovolt Res Appl* (2009) **17**, 372.
7. M.A. Green, M. A., et al. *Prog Photovolt Res Appl* (2010) **18**, 144.
8. www.energy-sunbags.de/index.php..
9. Sariciftci, N. S., *et al., Science* (1992) **258**, 1474.
10. Haugeneder, A., *et al., Phys Rev B* (1999) **59**, 15346.
11. Halls, J. J. M., *et al., Nature* (1995) **376**, 498.
12. Yu, G., *et al., Science* (1995) **270**, 1789.
13. Shaheen, S. E., *et al., Appl Phys Lett* (2001) **78**, 841.
14. Hoppe, H., and Sariciftci, N. S., *J Mat Chem* (2006) **16**, 45.
15. Yang, X., *et al., Macromolecules* (2004) **37**, 2151.
16. Coates, N. E., *et al., Appl Phys Lett* (2008) **93**, 072105.
17. Hoppe, H., *et al., Adv Funct Mater* (2004) **14**, 1005.
18. van Duren, J. K. J., *et al., Adv Func Mater* (2004) **14**, 425.
19. Padinger, F., *et al., Adv Funct Mater* (2003) **13**, 85.
20. Waldauf, C., *et al., Thin Solid Films* (2004) **451-452**, 503.
21. Al-Ibrahim, M., *Appl Phys Lett* (2005) **86**, 201120.
22. Reyes-Reyes, M., *et al., Appl Phys Lett* (2005) **87**, 083506.
23. Ma, W., *et al., Adv Funct Mater* (2005) **15**, 1617.
24. Friedrich, H., *et al., Chem Rev* (2009) **109**, 1613.
25. Midgley, P. A., *et al., Chem Soc Rev* (2007) **36**, 1477.
26. Weyland, M., and Midgley, P. A., *Mater Today* (2004) **7**, 32.
27. Jinnai, H., and Spontak, R. J., *Polymer* (2009) **50**, 1067.
28. Jinnai, H., *et al., Macromolecules* (2010) **43**, 1675.
29. van Bavel, S. S., and Loos, J., *Adv Func Mater* In press.
30. Möbus, G., and Inkson, B. J., *Mater Today* (2007) **10**, 18.
31. Cormack, A. M., *J Appl Phys* (1963) **34**, 2722.
32. Crowther, R. A., *et al., Proc R Soc London A* (1970) **317**, 319.
33. Gilbert, P. F. C., *Proc R Soc London B* (1972) **182**, 89.
34. Gilbert, P. F. C., *J Theor Biol* (1972) **36**, 105.
35. Prosa, T. J., *et al., Macromolecules* (1992) **25**, 4364.
36. Mihailetchi, V. D., *et al., Adv Funct Mater* (2006) **16**, 599.
37. Mihailetchi, V. D., *et al., Adv Funct Mater* (2003) **13**, 43.
38. Yang, X., *et al., Adv Mater* (2004) **16**, 802.
39. van Bavel, S. S., *et al., Nano Lett* (2009) **9**, 507.
40. van Bavel, S. S., *et al., Macromolecules* (2009) **42,** 7396.
41. Campoy-Quiles, M., *et al., Nat Mater* (2008) **7**, 158.
42. Xu, Z., *et al., Adv Funct Mater* (2009) **19**, 1227.
43. Germack, D. S., *et al., Macromolecules* (2010) **43**, 3828.
44. Huynh, W. U., *et al., Science* (2002) **295**, 2425.
45. Wang, P., *et al., Nano Lett* (2006) **6**, 1789.
46. Kwong, C. Y., *et al., Chem Phys Lett* (2004) **384**, 372.
47. Kuo, C. Y., *et al., Appl Phys Lett* (2008) **93**, 033307.
48. Beek, W. J. E., *et al., Adv Mater* (2004) **16**, 1009.
49. Beek, W. J. E., *et al., Adv Funct Mater* (2006) **16**, 1112.
50. Olson, D. C., *et al., J Phys Chem C* (2007) **111**, 16640.
51. Oosterhout, S. D., *et al., Nat Mater* (2009), **8**, 818.
52. Hayakawa, A., *et al., Appl Phys Lett* (2007) **90**, 163517.
53. Hansel, H., *et al., Adv Mater* (2003) **15**, 2056.
54. Gilot, J., *et al., Appl Phys Lett* (2007) **91**, 113520.
55. Kim, J. Y., *et al., Science* (2007) **317**, 222.
56. Gilot, J., *et al., Appl Phys Lett* (2007) **90**, 143512.
57. Hadipour, A., *et al., Adv Funct Mater* (2006) **16**, 1897.
58. de Bettignies, R., *et al., Synth Met* (2006) **156**, 510.
59. Al-Ibrahim, M., *et al., Sol. Energy Mater Sol Cells* (2005) **85**, 13.
60. Conings, B., *et al., Appl Phys Lett* (2010) **96**, 163301.
61. Jorgensen, M., *et al., Sol Energy Mater Sol Cells* (2008) **92**, 686.
62. Loos, J., *et al., Polymer* (2002) **43**, 7493.
63. van Duren, J. K. J., *et al., Adv Func Mat* (2002) **12**, 665.